Dalton
Transactions

An international journal of inorganic chemistry

rsc.li/dalton

ROYAL SOCIETY
OF CHEMISTRY
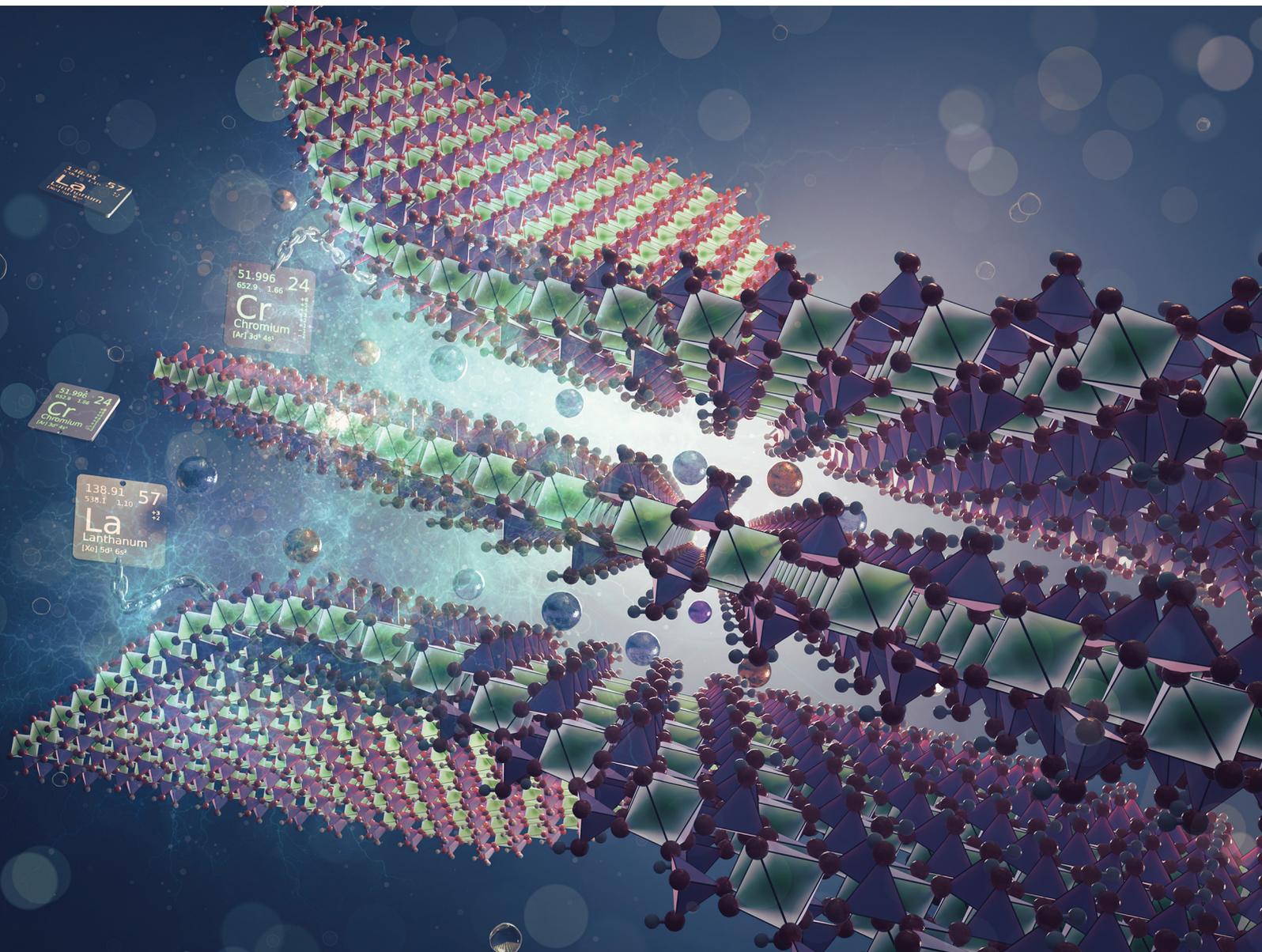
PAPER
Jonathan D. Burns *et al.*
Uptake and binding of La³⁺ and Cr³⁺ ions by alkali metal
substituted alpha-zirconium phosphate

Check for updates

Uptake and binding of La³⁺ and Cr³⁺ ions by alkali metal substituted alpha-zirconium phosphate

B. D. Imansha Madhushan, Adrianna L. Orsi, Jennifer M. Pyles [ID] and Jonathan D. Burns [ID] *

The conversion of alpha-zirconium phosphate, $Zr(HPO_4)_2 \cdot H_2O$, to the K-, Rb-, and Cs-phases and the subsequent ion exchange behavior of these alkali metal phases, A-ZrP, with La^{3+} and Cr^{3+} have been investigated. The conversion to the A-ZrP phases was achieved by reaction with metal chloride, metal hydroxide solution, and confirmed through various techniques, including X-ray powder diffraction, thermogravimetry analysis, IR spectroscopy, scanning and transmission electron microscopy, and X-ray photoelectron spectroscopy. The effect of material hydration, which increased the interlayer distance, was also examined. The ion exchange behavior of the A-ZrP showed strong affinity for both La^{3+}, a representative for trivalent lanthanide metals, and Cr^{3+}, a representative for the trivalent transition metals, with a rapid, near quantitative removal of the M^{3+} ions at a pH of 3 when the ion concentration was ≤25% of the ion exchange capacity of the materials. Additionally, the ion affinity was shown to be pH and concentration-dependent, decreasing with a decrease in pH or an increase in ion concentration. Lastly, the binding strength of La- and Cr-loaded ZrP materials was examined through a series of leaching experiments in a carbonate buffer, phosphate buffer, HEPES buffer, and a series of EDTA solutions at various concentrations. No observable leaching occurred in the carbonate buffer, phosphate buffer, HEPES buffer, or when the EDTA concentration was below 0.1 mM. These results highlight the potential for the A-ZrP materials to provide a platform for trivalent transition metal and trivalent lanthanide radionuclide capture for various applications.

Introduction

Targeted radionuclide therapy (TRT) for the treatment of various kinds of cancer relies on the idea of linking a radionuclide to certain carrier molecules that are tumor-selective, thereby targeting the cancer with emitted radiation.[1] These tumor-seeking molecules are the delivery mechanism or vehicle in which the radionuclide is transported to the tumor. Once delivered, the radiation emitted from the radionuclide can either be used to image and diagnose or can be used for therapy as a cytotoxin to eliminate the cancerous cell, and in some cases, simultaneously fulfill both roles; a so-called theranostic.[2]

As is the case with all drug delivery mechanisms, the problem of administering the cytotoxin to the cancer cells or tumor and avoiding distribution to healthy cells becomes one of the largest hurdles to cross. Like nonradioactive cytotoxic drugs, the challenge of targeting the desired cells is very important and relies heavily on the biochemistry of marker molecules, which can range from a variety of antibodies, pep-

tides, proteins, or other organic molecules. However, unlike other cytotoxic drugs, TRT drugs have the added requirement of being resistant to radiation. This limits the strategy for designing the delivery mechanism, as many ligands are susceptible to radiolysis. One approach to combating this is to use an inorganic material as the host of the radionuclide. An exciting alternative to the use of chelators is to employ nanoparticles and exploit some of the unique properties they exhibit.[3] A variety of materials have been studied with limited success, ranging from carbon nanotubes,[4] lanthanum phosphate nanoparticles,[5] lanthanum vanadate nanoparticles,[6,7] and polymer-based nanoparticles,[8] as well as zirconium phosphate-based materials.[9,10]

The acidic, ion exchange material, alpha-zirconium phosphate (α-ZrP), with a composition $Zr(HPO_4)_2 \cdot H_2O$, has great potential as a radionuclide delivery vehicle.[9,10] It has a layered structure with Zr atoms that are arranged in a nearly planar configuration. The Zr atoms are octahedrally coordinated by six O_3POH^{2-} groups through one of the O atoms. Each O_3POH^{2-} group is bound to three Zr atoms in this fashion. Each O_3POH^{2-} group is bound to the layer by three O atoms, with the fourth O, as an OH group, pointing towards the interlayer space. The layers are H-bonded together by the crystalline

Department of Chemistry, University of Alabama at Birmingham, Birmingham, AL 35294, USA. E-mail: burnsjon@uab.edu

H_2O molecule, resulting in an interlayer distance of 7.6 Å. The acidic nature of the material comes from the OH group, where the proton can participate in ion-exchange reactions. The ion exchange properties of α-ZrP have been a topic of much interest since its discovery in 1964.[11] The total ion-exchange capacity (IEC) is 6.64 mEq g^{-1},[12] which is a much larger capacity than traditional ion exchangers like Dowex 50, which only has ~1.7 mEq g^{-1}.

Other benefits for investigating α-ZrP as a radionuclide delivery vehicle include: (1) it has a known crystal structure;[13,14] (2) it can be synthesized in extremely high purity (>99.99%);[12] (3) it has a nano-platelet shape;[12,15] (4) the surface is chemically modifiable;[16–21] (5) it has minimal or no cytotoxicity and no competing metabolic function;[22,23] and (6) it is stable under biological conditions. Another attractive property is that the particle size can be tuned synthetically.[17,24] The platelet-like shape of α-ZrP has the potential to maintain better adhesion, margination, and binding properties over other nanomaterials that have spherically shaped particles. For example, once loaded with the radionuclides, α-ZrP nano-platelets may reach the tumor by an enhanced permeability and retention (EPR) effect of cancerous tissues, enter into the cell *via* endocytosis, and release the radionuclide (*via* ion-exchange) under the acidic conditions of the endosomes and lysosomes. Overall, the physical properties, particle shape and size, along with the chemical properties, ion-exchange intercalation chemistry, and the ability to functionalize the surface, makes α-ZrP very attractive for radionuclide delivery.

The potential utility of α-ZrP as a drug delivery mechanism has previously been investigated for nonradioactive anti-cancer drugs like cisplatin (cisPt)[25] and doxorubicin (DOX).[15] The loading of cisPt was quite high, with one cisPt per formal unit of α-ZrP. The cisPt-loaded ZrP were tested with breast cancer cells, showing favorable uptake and cytotoxic properties. The larger DOX required the use of θ-phase, which has an inter-layer distance of ~10.3 Å to facilitate intercalation, but was shown to be incorporated at 35% w/w. The cytotoxicity and cell uptake of the DOX-loaded ZrP were improved compared to free DOX, while the α-ZrP alone had no measurable cytotoxicity. Loading surface-modified α-ZrP has previously been demonstrated with the intercalation of DOX into particles modified with PEG chains.[19] The combination of surface modification and intercalation makes this robust inorganic material attractive as a potential vehicle in radionuclide delivery.

More recently, we have shown, through proof-of-concept studies, the quantitative loading of ZrP with natural La^{3+}—a nonradioactive surrogate for $^{225}Ac^{3+}$—at pH 2, following a pseudo second-order diffusion model with a rate of 8.9 ± 0.4 g $mmol^{-1}$ h^{-1}.[9] Moreover, ZrP loaded with La^{3+}, along with surrogate daughter species of the ^{225}Ac decay chain, natural Cs^+ for $^{221}Fr^+$ and natural Bi^{3+} for $^{213}Bi^{3+}$, possessed a favorable *in vitro* release profile of the adsorbed ions in a human plasma buffer analog (10 mM carbonate buffer at a pH of 7.4), with less than 1% release of the ions over a 24 h period. This indicates the radionuclides will not leach from the layers during transport to the cancerous cells or tumor.

In this work, we examine the conversion of α-ZrP to the K-ZrP, Rb-ZrP, and Cs-ZrP phases, and their subsequent ion-exchange behavior towards trivalent lanthanides and transition metals. The uptake as a function of pH and the ratio of free ion concentration to ion exchange capacity were of particular interest. The binding strength of loaded materials was studied through a series of leaching studies.

Experimental

Materials

Nitric acid (ACS Grade, 68–70%, HNO_3), potassium chloride (ACS Grade, 95–99.5%, KCl), potassium hydroxide (ACS Grade, 100%, KOH), nitric acid (Omnitrace® trace metal analysis, 67–70%, HNO_3) were purchased from VWR Chemicals BDH; phosphoric acid (ACS Grade, 85%, H_3PO_4), chromium(III) nitrate nonahydrate (ACS grade, 98.5%, $Cr(NO_3)_3 \cdot 9H_2O$), and tampon phosphate pH 7.2 buffer (ACS Grade) were purchased from VWR Chemicals; cesium hydroxide 50% solution water (Trace metal basis for analysis, 99.9%, CsOH) and zirconyl chloride octahydrate (ACS Grade, 98%, $ZrOCl_2 \cdot 8H_2O$) were purchased from Acros Organics; rubidium hydroxide 50% w/w aqueous solution (metal basis, 99.6%, RbOH), rubidium chloride (trace metal basis, 99.8+%, RbCl), cesium chloride (ultrapure, 99.9% metal basis, CsCl), and 4-(2-hydroxyethyl)-1-piperazineethanesulfonic buffer pH 7.2 (ACS Grade, HEPES) were purchased from Thermo Scientific; ethylenediaminetetraacetic disodium(ACS Grade, EDTA) was purchased from Fisher Chemical company; sodium bicarbonate (ACS Grade,7.5% w/v, $NaHCO_3$) was purchased from Quality Biological; lanthanum chloride heptahydrate (ACS Grade, $LaCl_3 \cdot 7H_2O$) was purchased from Sigma Chemical company; and all were used as received. Deionized (DI) H_2O was obtained from an ELGA LabWater Purelab Flex ultrapure laboratory water purification system operated at 18.2 MΩ cm at 25 °C.

Methods

X-ray powder diffraction (XRPD) patterns were collected on a Panalytical Empyrean X-ray diffractometer with copper X-ray source (λ = 1.5406 Å), carried out at 45 kV and 40 mA, with a scan range of 5–45° 2θ by the reflection-transmission spinner method (step 0.013°, time 0.1 s). Thermogravimetry analysis (TGA) was performed using a PerkinElmer Thermogravimetric Analyzer TGA 8000 at a heating rate of 5 °C per min up to 800 °C under N_2 airflow. Attenuated total reflectance Fourier transform infrared (ATR-FT-IR) analyses were done by using a PerkinElmer Spectrum Two™ FT-IR Spectrometer and Analysis Systems equipped with a PIKE Technologies Inc. MIRacle™ ATR diamond crystal plate single reflection accessory from 500–4000 cm^{-1}, averaging 16 scans per spectrum. Scanning electron microscopy (SEM) measurements were performed on a FEI Quanta 650 FEG scanning electron microscope. The SEM electron beam was operated at an accelerating voltage of 5 kV, and the images were recorded from the secondary electron (SE) detector signal. SEM data was collected using XT micro-

scope control software. Samples were sputtered using Denton Desk V with a platinum/palladium target. Transmission electron microscopy (TEM) analysis was performed using a JEOL 1400 flash electron-Ins microscope. The beam energy for the electron was 120 kV. An AMT-NanoSprint43L-MarkII Camera was used to take the image. X-ray photoelectron spectroscopy (XPS) was performed using the Phi Electronics VersaProbe 5000 spectrometer, featuring a micro-focused AI monochromatic source (λ = 1486.6 eV) and a dual anode conventional X-ray source equipped with a neutralizer. Survey spectra were captured with a step size of 0.8 eV and pass energy of 187.85 eV, while high-resolution scans had a step size of 0.1 eV with a pass energy of 23.5 eV. Inductively coupled plasma optical emission spectroscopy (ICP-OES) was performed using Agilent 5800 Inductively Coupled Plasma OES to determine the concentration of metal ions in solution.

Synthesis of alpha-zirconium phosphate

alpha-Zirconium phosphate (α-ZrP) was synthesized on the 5-g scale under hydrothermal conditions using a Tosyuwir 100-mL hydrothermal synthesis autoclave reactor equipped with polypropylene (PPL) liner. The general procedure was to dissolve 5.336 g of $ZrOCl_2 \cdot 8H_2O$ in 20 mL of H_2O in the PPL liner. While stirring, 30 mL of 4 M H_3PO_4 was added dropwise. The final ratio of P : Zr was roughly 7.25 : 1. Once mixed, the PPL liner was sealed in the hydrothermal synthesis autoclave reactor and heated at 200 °C for 6 h in a VWR forced air oven. The reactor was then removed from the oven and allowed to cool overnight. The product was then washed with H_2O followed by centrifugation and decantation of the supernate. Several washes were conducted to remove the excess H_3PO_4. The powder was dried at 30 °C for 24 h. The resulting white solid was then ground to a fine powder with a mortar and pestle.

Conversion of alpha-zirconium phosphate to the alkali metal substituted phases

The α-ZrP was converted to the A-phase, where A = K, Rb, or Cs, by reaction with an AOH-ACl solution. The general procedure was to contact 1 g (~3.3 mmol) of α-ZrP with 70 mL of 0.1 M AOH and 0.1 M ACl solution inside a 250 mL beaker for two weeks, followed by centrifugation and decantation of the supernate. This process was repeated until the final pH of the supernate of 10.2 was achieved. As with the α-ZrP, the product was then washed with H_2O followed by centrifugation and decantation of the supernate. Several washes were conducted to remove the excess AOH and ACl and the product was dried at 30 °C or 65 °C for 24 h. The resulting white solid was then reground to a fine powder with a mortar and pestle.

Ion exchange reactions with alkali metal substituted alpha-zirconium phosphate phases

Batch ion exchange studies were conducted by contacting roughly 50 mg of the A-ZrP material with 1.0 mL of La^{3+} or Cr^{3+} at 85 °C for 5 min, where the cation concentration was a fraction of the IEC, of 0.25 (8.9–13 mM), 0.50 (19–30 mM), 0.75

(25–46 mM), and 1.00 (38–58 mM) Eq per IEC. The pH dependence was also studied by adjusting the pH to 1–3 using HCl. The mixture was continuously stirred using magnetic stir plates in a 15-mL centrifuge tube on a hot plate. After 5 min, the mixture was centrifuged, and an aliquot was sampled, diluted, and analyzed by ICP-OES. The ion exchange was measured by calculating the distribution coefficient (eqn (1)), K_d, and the percent removal (eqn (2)), $R\%$,

$$K_d = \frac{[M]_I - [M]_{Eq}}{[M]_{Eq}} \cdot \frac{V}{m} \quad (1)$$

where $[M]_I$ and $[M]_{Eq}$ are the concentration of La^{3+} or Cr^{3+} before and after contact with the A-ZrP materials, respectively, V is the volume of metal solution in mL, and m is the mass of the exchanger in g.

$$R\% = \frac{[M]_I - [M]_{Eq}}{[M]_I} \times 100\% \quad (2)$$

Leaching of the La^{3+} and Cr^{3+} loaded alkali metal substituted alpha-zirconium phosphate phases

Batch leaching experiments of the La^{3+} and Cr^{3+} loaded A-ZrP materials were conducted by taking *ca.* 50 mg of the A-ZrP material and contacting it with a 2 mM Cr^{3+} or 7 mM La^{3+} solution at pH of 2.8 or 3.2, respectively, for 5 min. The supernate was then removed by centrifugation and decantation. To the resulting Cr^{3+} and La^{3+} loaded A-ZrP solid, 1 mL of leaching solution (see Table 1) was added, and the two phases were mixed by using magnetic stir plates in a 15 mL centrifuge tube for 24 h at 20 °C. The samples were then centrifuged, and an aliquot was sampled and analyzed by ICP-OES. The leaching was measured by calculating the percent leached (eqn (3)), $L\%$,

$$L\% = \frac{M_{aq\,Eq}}{M_{s\,Eq} + M_{aq\,Eq}} \quad (3)$$

where M_{aq} and M_s are the mass of metal in solution and the loaded A-ZrP materials, respectively.

Results and discussion

Synthesis and characterization of A-ZrP materials

To begin with, the A-ZrP phases were synthesized *via* a reaction of the pristine α-ZrP with metal hydroxide and metal chloride solutions. To accomplish this, the pristine α-ZrP was systemati-

Table 1 Details of leaching solutions

Buffer	Concentration	pH
Carbonate	8.9 mM	7.4
Phosphate	100 mM	7.2
HEPES	10 mM	7.4
10 mM EDTA	10 mM	7.2
1.0 mM EDTA	1.0 mM	7.3
0.1 mM EDTA	0.10 mM	7.2

cally titrated with the different metal solutions, as shown in Fig. 1. In all three cases, two equivalence points were observed, indicating the replacement of the two acidic protons of the α-ZrP (see Table 2). The conversion of the pristine α-ZrP to the K-ZrP phase followed the expected behavior, with the first equivalence point, EP1, occurring near the half IEC of α-ZrP, 3.4 ± 0.3 mEq g^{-1}, and the second equivalence point, EP2, occurring near the IEC of α-ZrP, 6.4 ± 0.3 mEq g^{-1}. The conversion to both the Rb-ZrP and Cs-ZrP phases showed a much different behavior. The first equivalence point for the exchange of Rb occurred much sooner at 0.9 ± 0.3 mEq g^{-1}, and for the Cs, even earlier, 0.4 ± 0.4, while the second equivalence points were 6.6 ± 0.3 and 6.1 ± 0.4, respectively. These results align with what Kullberg et al.[26] and Alberti[27] observed and indicate the formation of a solid solution with the ZrP materials. The Cs-ZrP material was not fully converted to the Cs-phase, with the second equivalence point only reaching 6.1 ± 0.4. This is expected as the large size of the Cs$^+$ will prevent the Cs$^+$ from packing efficiently, leaving a portion of the phosphate groups protonated.

Following the conversion of the pristine α-ZrP to the various A-ZrP phases, the materials were recovered and dried using two different temperatures, 30 °C (hydrated), and 65 °C (dry). This was carried out to determine the effect hydration had on the ion exchange properties. With the exception of the Cs-ZrP material dried at 65 °C, once dry, the resulting white solids were easily ground into a free-flowing powder. The Cs-ZrP material dried at 65 °C was very hard and did not grind well, requiring excessive force to break up the white solid into a powder. As will be discussed in a later section, this is believed to be a result of the nanoplatelets fusing together and shattering as they were ground. Each material was then characterized by a variety of techniques.

To begin with, XRPD was performed to confirm that the larger cations were being intercalated between the layers. As can be seen in Fig. 2, the hydrated materials show an increase

Table 2 Observed equivalence points (EPs) during the conversion of the pristine α-ZrP phase to the K-ZrP, Rb-ZrP, and Cs-ZrP phases by titration with a solution of 0.1 M MOH and 0.1 M MCl

Sample	EP 1 (mEq g^{-1})	EP 2 (mEq g^{-1})
K-ZrP	3.4 ± 0.3	6.4 ± 0.3
Rb-ZrP	0.9 ± 0.3	6.6 ± 0.3
Cs-ZrP	0.4 ± 0.4	6.1 ± 0.4

in the *d*-spacing of the 002 reflection from 7.5 Å to 10.7 Å, 10.6 Å, and 11.6 Å when the H$^+$ is exchanged with K$^+$, Rb$^+$, and Cs$^+$, respectively, as summarized in Table 3. Additionally, as the ion size increased the intensity of the reflections in the powder patterns decreased, indicating the materials were becoming more amorphous as the distance increased. One reason for this is certainly a result of the disruption of the H-bonding network that is present in the pristine α-ZrP. Without the H-bonding network, the layers are not bound as tightly, which will allow more variation. This is also complicated by the fact that the interlayer space is filled with a double layer of cations, contributing to a decrease in the long-range order of the materials. The dry materials show similar changes in their diffraction patterns as the hydrated materials (see Fig. 3), except that the *d*-spacing was smaller, 9.0 Å and 9.3 Å, for the K-ZrP and Rb-ZrP, respectively. This is an expected result, as a higher drying temperature will drive off excess water residing between the layers. This will be discussed in detail below with the TGA results. The dry Cs-ZrP did not have an observable 002 reflection plane in the powder pattern, which could be caused by a complete disruption of the order of the layering or could be evidence of a structural change in the material altogether.

Next, the TGA measurements were obtained on both the hydrated and the dry (see Fig. 4 and 5) materials. All six A-ZrP materials showed two weight losses, the first around 100 °C,
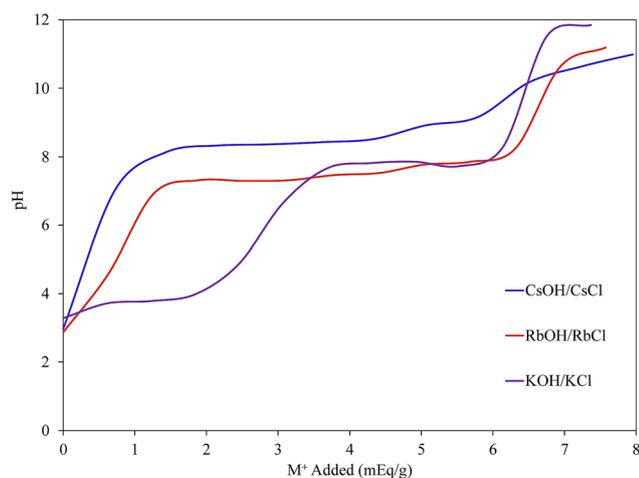
Fig. 1 Conversion of the pristine α-ZrP phase to the K-ZrP, Rb-ZrP, and Cs-ZrP phases by titration with a solution of 0.1 M MOH and 0.1 M MCl.
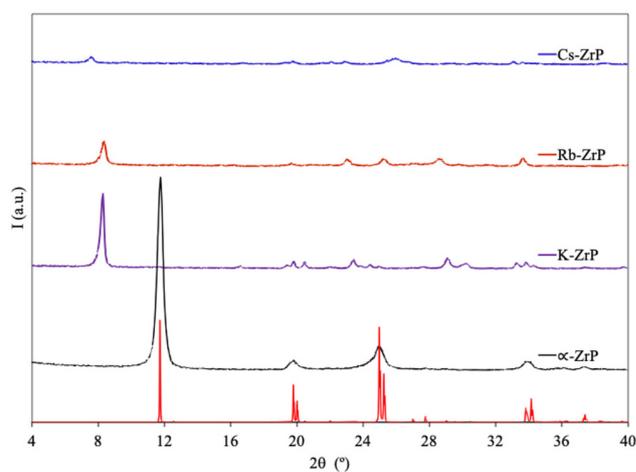
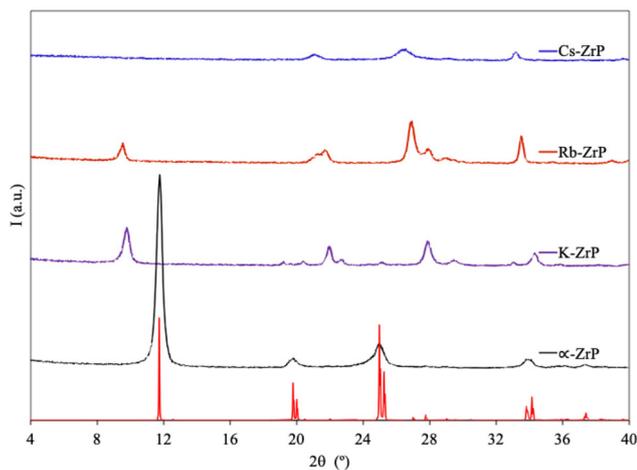**Fig. 2** Powder X-ray diffraction patterns of the pristine α-ZrP and the hydrated K-ZrP, Rb-ZrP, and Cs-ZrP phases. The red lines indicate the calculated pattern from the crystal structure of Zr(O$_3$POH)$_2$·H$_2$O.[13]

Table 3 Observed *d*-spacing for the 002 reflections planes of the pristine α-ZrP and the hydrated and dry K-ZrP, Rb-ZrP, and Cs-ZrP phases

Sample	2θ (002)	d-Spacing (Å)
α-ZrP	11.75	7.5
K-ZrP hydrated	8.28	10.7
K-ZrP dry	9.79	9.0
Rb-ZrP hydrated	8.34	10.6
Rb-ZrP dry	9.53	9.3
Cs-ZrP hydrated	7.64	11.6
Cs-ZrP dry	—	—

Fig. 3 Powder X-ray diffraction patterns of the pristine α-ZrP and the dry K-ZrP, Rb-ZrP, and Cs-ZrP phases. The red lines indicate the calculated pattern from the crystal structure of $Zr(O_3POH)_2 \cdot H_2O$.[13]
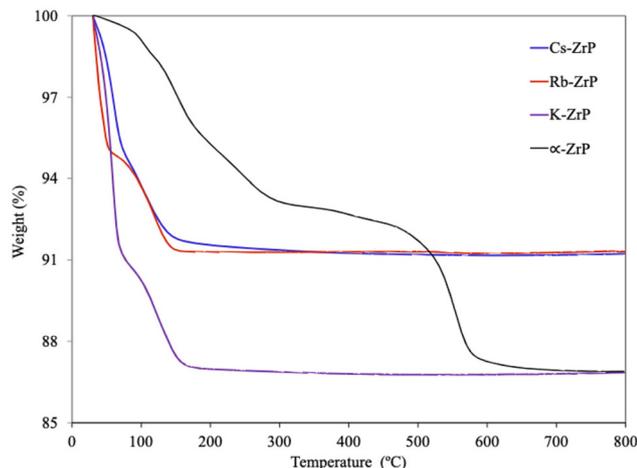
Fig. 4 Thermogravimetric analysis of the pristine α-ZrP and the hydrated K-ZrP, Rb-ZrP, and Cs-ZrP phases.

which is presumably loosely bound surface water. While the second is around 200 °C, which is believed to be more strongly bound water present between the layers. As summarized in Table 4, the largest difference between the two sets of materials was in the first loss, which is not unexpected, as the
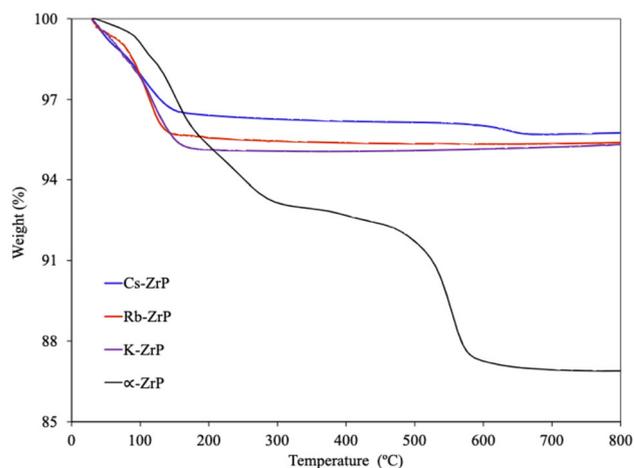
Fig. 5 Thermogravimetric analysis of the pristine α-ZrP and the dry K-ZrP, Rb-ZrP, and Cs-ZrP phases.

dry materials should have a lower water content. The hydrated K-ZrP had the largest water content, ~13.2%, followed by the hydrated Rb-ZrP and Cs-ZrP materials at ~8.7%. For the dry materials, the K-ZrP and Rb-ZrP both showed a water content of ~4.6%, while the dry Cs-ZrP material had a water content of ~3.6% and an additional 0.65% loss from 600–660 °C, which is indicative of incomplete conversion from the α-phase and is believed to be the condensation of residual –OH groups. This is in line with previous reports by Kullberg *et al.*[26] and Alberti,[27] where the large size of the Cs^+ does not allow for close packing of the cations, so some portion of the smaller H^+ remains to charge balance the material. The hydrated Cs-ZrP material did show a very subtle, <0.5%, higher temperature loss, which starts between 250–300 °C and extends up to roughly 500 °C. At this point, it is not clear why the hydrated Cs-ZrP material shows the condensation loss at lower temperatures. One explanation could be that there is a lower diffusion barrier, due to the larger *d*-spacing of Zr layers.

From the titration, powder XRD, and the TGA, the chemical formulas and percent yield of the conversion were calculated (see Table 5). The yields were on the order of 80–90%. This is a little lower than expected and is believed to be due to the copious washing required to remove the excess hydroxide solution, which inevitably leads to some loss of the material. The hydrated materials have 2.4–3.2 mols of H_2O per unit formula, while the dry materials have roughly 1.0–1.2 mols of H_2O per

Table 4 Summary of the TGA weight loss for the hydrated and dry K-ZrP, Rb-ZrP, and Cs-ZrP phases

Sample	0–100 °C	100–200 °C	Total
K-ZrP hydrated	9.77%	3.25%	13.15%
K-ZrP dry	2.19%	2.69%	4.68%
Rb-ZrP hydrated	6.30%	2.41%	8.69%
Rb-ZrP dry	2.15%	2.29%	4.61%
Cs-ZrP hydrated	6.29%	2.16%	8.78%
Cs-ZrP dry	2.08%	1.51%	4.24%

**Table 5** Summary of the characterization and analysis of the A–ZrP materials

Sample	Formula	n	FW	%Yield
K-ZrP hydrated	$Zr(O_3POK)_2 \cdot nH_2O$	3.2	416	85.8%
K-ZrP dry	$Zr(O_3POK)_2 \cdot nH_2O$	1.0	377	91.2%
Rb-ZrP hydrated	$Zr(O_3PORb)_2 \cdot nH_2O$	2.4	495	85.9%
Rb-ZrP dry	$Zr(O_3PORb)_2 \cdot nH_2O$	1.2	474	86.4%
Cs-ZrP hydrated	$Zr(O_3POH)_{0.1}(O_3POCs)_{1.9} \cdot nH_2O$	2.9	587	83.2%
Cs-ZrP dry	$Zr(O_3POH)_{0.1}(O_3POCs)_{1.9} \cdot nH_2O$	1.1	554	80.5%

unit formula. This leads to the hydrated materials having noticeably higher formal weights.

The ATR-FT-IR spectra were then obtained for both the hydrated and dry materials and are shown in Fig. 6 and 7, respectively. Upon converting the pristine α-ZrP materials to the K-, Rb-, and Cs-phase, the crystalline water vibrations at 3510 cm^{-1} and 3592 cm^{-1} disappeared, and for the hydrated materials, were replaced by broad water bands from 2700–3700 cm^{-1}. The dry materials, on the other hand, showed very little water content in the 2700–3700 cm^{-1} region, as expected. Similarly, the water bending vibration at 1618 cm^{-1} in the pristine α-ZrP shifts to higher wavenumber, 1646 cm^{-1}, 1671 cm^{-1}, and 1679 cm^{-1}, and progressively decreases in intensity for the K-, Rb-, and Cs-ZrP materials, respectively, for the hydrated materials. Likewise, the dry materials also shifted to higher wavenumber, 1652 cm^{-1}, 1675 cm^{-1}, and 1682 cm^{-1}, and progressively decreased in intensity for the K-, Rb-, and Cs-ZrP materials, respectively. The out-of-plane bending vibration of the P–OH at 1250 cm^{-1} in α-ZrP decreases in intensity and shifts to a lower wavenumber, between 1185–1195 cm^{-1}, for both the hydrated and dry materials. This is expected, as the deprotonated P–O$^-$ group will no longer be involved in H-bonding, allowing it to move
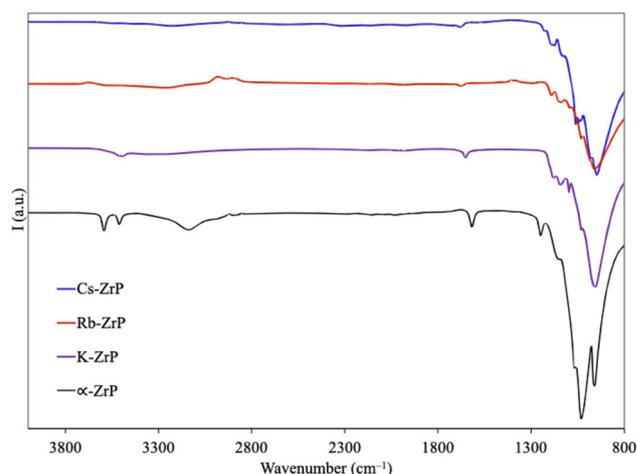
Fig. 7 Attenuated total reflectance Fourier transform infrared analysis of the pristine α-ZrP and the dry K-ZrP, Rb-ZrP, and Cs-ZrP phases.

more freely. Upon exchanging the H$^+$ with K$^+$, Rb$^+$, or Cs$^+$, the POH stretch at 1030 cm^{-1} almost completely disappears, as expected.

Fig. 6 Attenuated total reflectance Fourier transform infrared analysis of the pristine α-ZrP and the hydrated K-ZrP, Rb-ZrP, and Cs-ZrP phases.
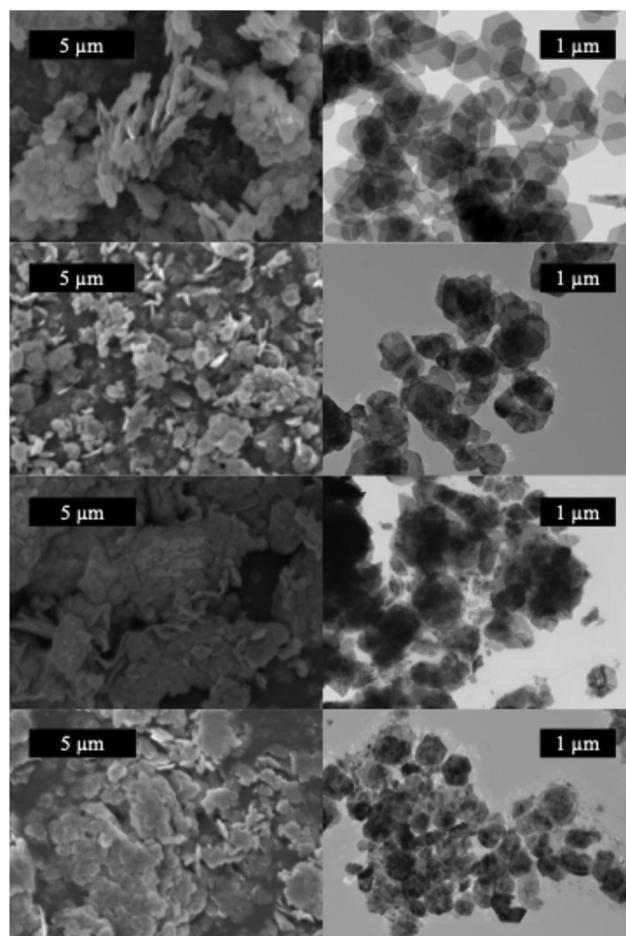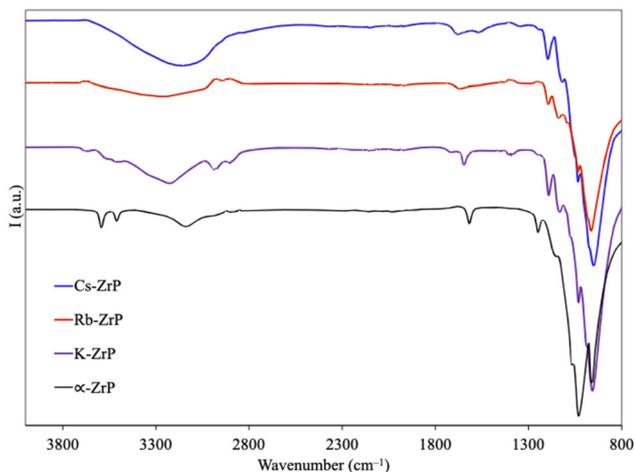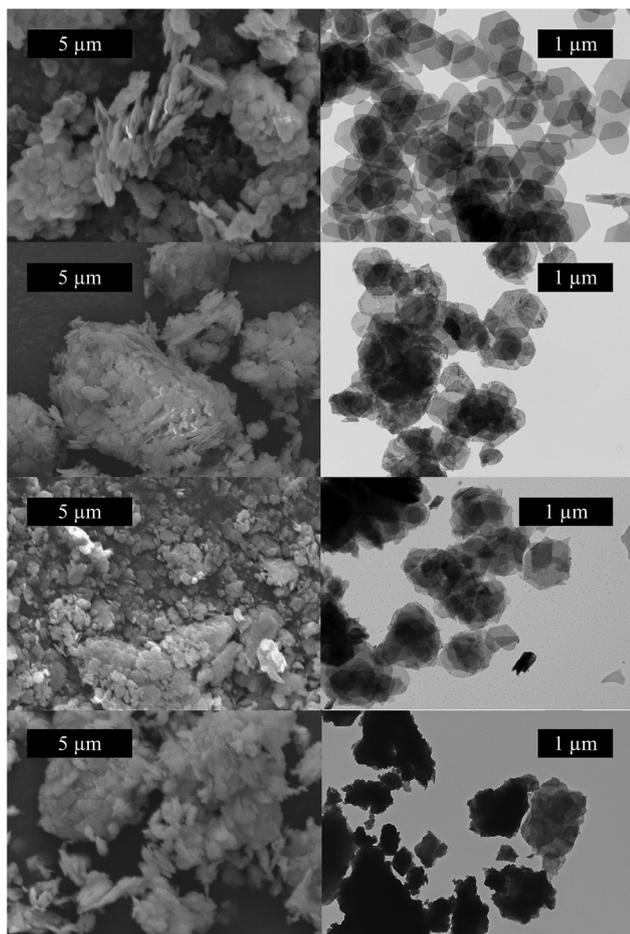

Fig. 8 SEM (left column) and TEM (right column) of the pristine α-ZrP (top row) and the hydrated K-ZrP (upper middle row), Rb-ZrP (lower middle row), and Cs-ZrP (bottom row) phases.

Fig. 9 SEM (left column) and TEM (right column) of the pristine α-ZrP (top row) and the dry K-ZrP (upper middle row), Rb-ZrP (lower middle row), and Cs-ZrP (bottom row) phases.

In all six materials, the particle size, shape, and morphology remain similar, regardless of the counter-cation, as observed in the SEM and TEM images, shown in Fig. 8 and 9. The hexagonal nanoplatelet showed a high aspect ratio of *ca.* 10, where the width of the particles was roughly 250–700 nm and the thickness was roughly 20–70 nm. This is in line with the previously discussed results, where the only thing that is changing about the material is a replacement of the H$^+$ in α-ZrP phase with the alkali metal cation in the A-ZrP phase. It should be noted that, slight degradation of the surface was observed for the Rb-ZrP and Cs-ZrP materials, as seen in the TEM images, which may indicate hydrolysis of the surface to a small extent. As the majority of the ion exchange sites are found in between the layers, the overall behavior is not expected to be altered significantly.

The XPS analysis further confirmed that no structural changes occur other than the exchange of H$^+$ for K$^+$, Rb$^+$, or Cs$^+$ and the subsequent expansion of the layers, as can be seen in Fig. 10 and 11. Only one Zr species was present, with the 3d$_{3/2}$ and 3d$_{5/2}$ signals at 181.3–182.4 eV and 183.7–184.3 eV, respectively, compared to the pristine α-ZrP Zr signals at
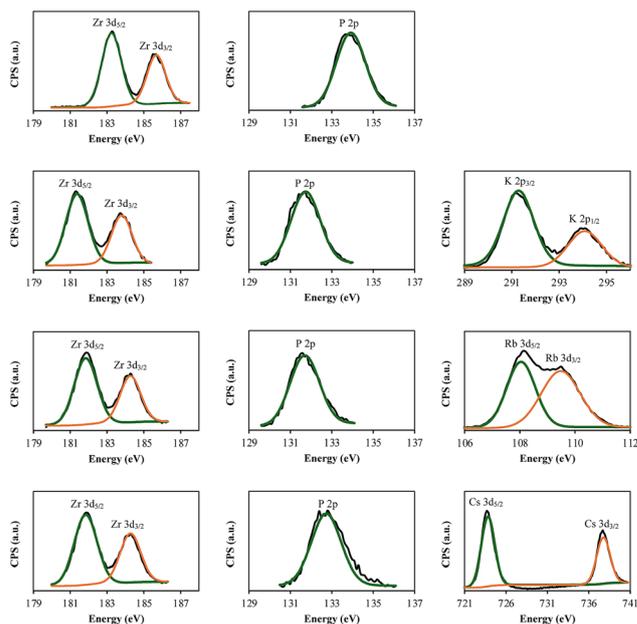

Fig. 10 XPS analysis of the pristine α-ZrP (top row) and the hydrated K-ZrP (upper middle row), Rb-ZrP (lower middle row), and Cs-ZrP (bottom row) phases.

183.3 eV and 185.7 eV. As with the Zr signals, the signals for P all showed a single species with the 2p signal at 131.7–132.7 eV, compared to the pristine α-ZrP P signal at 133.9 eV. All three of the counter cations, for K$^+$, Rb$^+$, and Cs$^+$, showed only a single species, as well. The P:Zr ratio remained approximately 2:1 in all cases (see Table 6). Again, this indicates the ions are intercalated between the layers in a uniform fashion.

Combined, all the characterization results indicate the ion exchange reaction occurred, resulting in the production of the K-, Rb-, and Cs-ZrP phases (see Table 5). The conversion of the A-ZrP phases did not produce any changes in the particle size, shape, or morphology, which resulted in the materials all having the same physical properties as the pristine α-ZrP. The incorporation of the larger ions did force the Zr layers further apart and should allow for much more rapid ion exchange without the need to add OH$^-$ to the system. This will be the focus of the next section.

Ion exchange reactions of A-ZrP materials

To begin with, La^{3+} was selected as a representative for the trivalent lanthanide metals and its removal from solution *via* ion exchange with both the hydrated and dry phases of K-ZrP, Rb-ZrP, and Cs-ZrP was studied (see Fig. 12 and 13). This included examining the ion exchange behavior as a function of solution pH and La^{3+} ion concentration. As expected, in all cases, the percent removal (%R) decreased with a decrease in solution pH. This is due to the H$^+$ concentration increasing and outcompeting the La^{3+} for the PO$^-$ active sites. Likewise, the general trend of %R decreased as the La^{3+} ion increased relative to the total number of ion exchange sites (%IEC). This is believed to be due to the system moving away from the thermo-
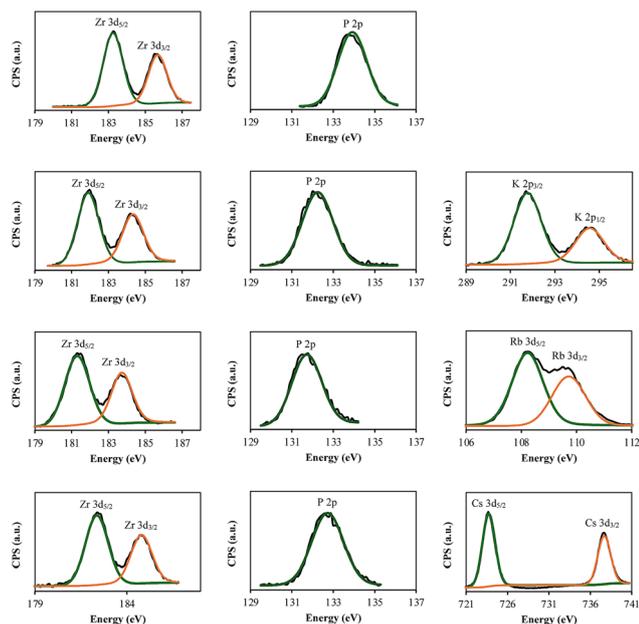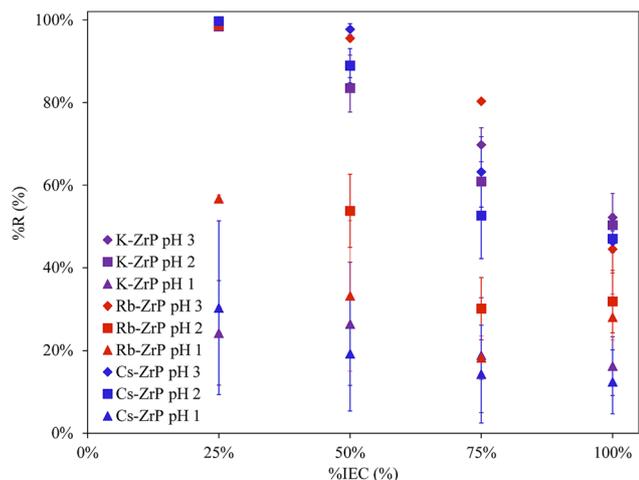
Fig. 11 XPS analysis of the pristine α-ZrP (top row) and the dry K-ZrP (upper middle row), Rb-ZrP (lower middle row), and Cs-ZrP (bottom row) phases.

Table 6 Summary of the XPS characterization for P and Zr in the A-ZrP materials

Sample	P (%)	Zr (%)	P : Zr
α-ZrP	15.8	7.2	2.2
K-ZrP hydrated	13.8	6.9	2.0
K-ZrP dry	13.7	6.8	2.0
Rb-ZrP hydrated	13.6	6.7	2.0
Rb-ZrP dry	12.7	5.6	2.3
Cs-ZrP hydrated	13.9	7.3	1.9
Cs-ZrP dry	10.8	5.5	2.0

Fig. 12 Percent removal (%R) of La^{3+} ions from solution present at 25%, 50%, 75%, and 100% of the IEC for the hydrated K-ZrP, Rb-ZrP, and Cs-ZrP phases.
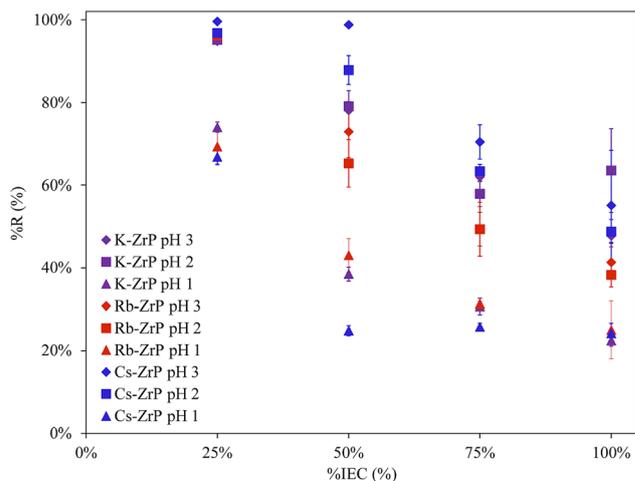
Fig. 13 Percent removal (%R) of La^{3+} ions from solution present at 25%, 50%, 75%, and 100% of the IEC for the dry K-ZrP, Rb-ZrP, and Cs-ZrP phases.

dynamically ideal case, where, when the ion concentration is low, every La^{3+} cation has an equal probability of interacting with an unoccupied PO^- active site, while when the relative concentration of the La^{3+} approaches the saturation limit, many of the PO^- active sites are occupied, restricting further interaction with free La^{3+}.

As seen in Tables 7 and 8, the affinity of La^{3+} for the hydrated phase is higher than that of the dry phase for all three materials, K-ZrP, Rb-ZrP, and Cs-ZrP. Of the three materials, the Cs-ZrP consistently showed the highest affinity for La^{3+}, followed by the Rb-ZrP and finally the K-ZrP. This is believed to be caused by two reasons. First, and probably the most impactful, comes from the difference in effective nuclear charge (Z_{eff}). The larger radii of the Cs^+ cation, while still maintaining the single "+" charge, reduces the charge density of the ion and reduces the electrostatic interaction with the PO^- active sites. While the Rb^+ and K^+ cations have progressively higher charge densities and are more strongly bound to the PO^- active sites. The second reason is that as the cation size increased from K^+ to Rb^+ to Cs^+, so does the *d*-spacing of the Zr layers, which in turn reduces the diffusion barrier, facilitating a more effective ion exchange reaction. These two properties combined make the ion exchange reaction more effective as the counter cation is changed from a lighter alkali metal to a heavier one.

Next, the removal of Cr^{3+} from solution *via* ion exchange was studied to understand how a trivalent transition metal would behave in these systems. Again, both the hydrated and dry phases of K-ZrP, Rb-ZrP, and Cs-ZrP were studied (see Fig. 14 and 15) as a function of solution pH and Cr^{3+} concentration. As with the La^{3+}, the %R of Cr^{3+} decreased with a decrease in solution pH. However, this decrease was negligible between pH 3 and pH 2, where the sorption of the Cr^{3+} was nearly identical. This is believed to be due to the fact that the ionic radius of Cr^{3+} (0.62 Å (ref. 28)) is roughly half that of La^{3+}
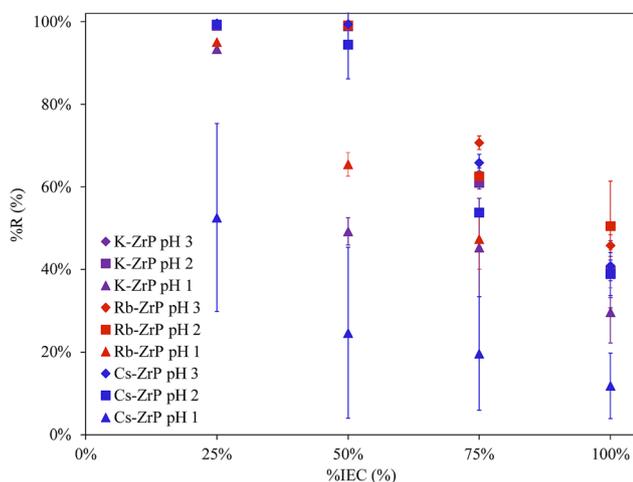
Table 7 Summary of the uptake of La^{3+} ions from solution present at 25%, 50%, 75%, and 100% of the IEC for the hydrated K-ZrP, Rb-ZrP, and Cs-ZrP phases

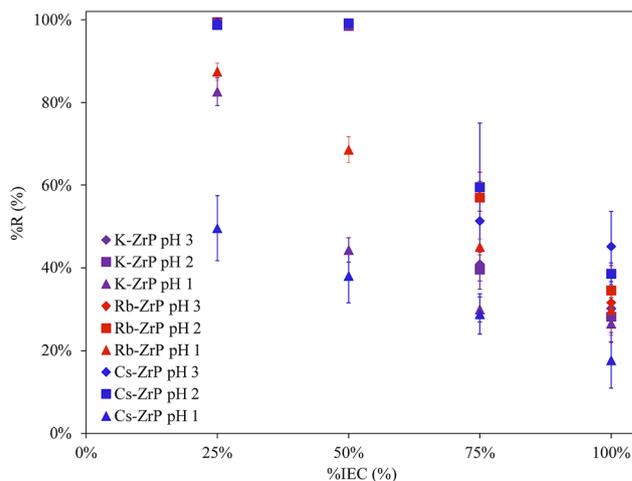| Sample	% IEC	pH 3 K_d (mL g^{-1})	pH 2 K_d (mL g^{-1})	pH 1 K_d (mL g^{-1})
K-ZrP	25%	2300 ± 1200	1200 ± 100	7 ± 4
	50%	160 ± 40	110 ± 50	8 ± 5
	75%	47 ± 9	30 ± 10	5 ± 4
	100%	22 ± 5	20 ± 2	4 ± 2
Rb-ZrP	25%	4900 ± 100	1500 ± 500	26 ± 1
	50%	430 ± 70	24 ± 9	11 ± 8
	75%	82 ± 1	9 ± 3	5 ± 2
	100%	16 ± 4	10 ± 3	8 ± 2
Cs-ZrP	25%	10 000 ± 5000	8000 ± 6000	10 ± 9
	50%	1000 ± 600	170 ± 70	5 ± 4
	75%	40 ± 10	20 ± 10	4 ± 3
	100%	17 ± 2	18 ± 2	3 ± 2

Table 8 Summary of the uptake of La^{3+} ions from solution present at 25%, 50%, 75%, and 100% of the IEC for the dry K-ZrP, Rb-ZrP, and Cs-ZrP phases

Sample	% IEC	pH 3 K_d (mL g^{-1})	pH 2 K_d (mL g^{-1})	pH 1 K_d (mL g^{-1})
K-ZrP	25%	400 ± 30	400 ± 30	57 ± 4
	50%	70 ± 20	80 ± 10	13 ± 1
	75%	33 ± 2	28 ± 4	9 ± 1
	100%	18 ± 1	37 ± 14	6 ± 1
Rb-ZrP	25%	600 ± 200	500 ± 0	50 ± 10
	50%	60 ± 20	39 ± 9	15 ± 2
	75%	20 ± 5	20 ± 3	9 ± 1
	100%	14 ± 2	12 ± 1	7 ± 3
Cs-ZrP	25%	5000 ± 2000	600 ± 50	40 ± 4
	50%	1600 ± 100	150 ± 50	7 ± 1
	75%	50 ± 10	35 ± 3	7 ± 1
	100%	30 ± 20	19 ± 2	6 ± 1

Fig. 14 Percent removal (%R) of Cr^{3+} ions from solution present at 25%, 50%, 75%, and 100% of the IEC for the hydrated K-ZrP, Rb-ZrP, and Cs-ZrP phases.

Fig. 15 Percent removal (%R) of Cr^{3+} ions from solution present at 25%, 50%, 75%, and 100% of the IEC for the dry K-ZrP, Rb-ZrP, and Cs-ZrP phases.

tion of Cr^{3+} dropped significantly, as the H^+ began to outcompete the Cr^{3+} for the PO^- active sites. Much like the case with the La^{3+}, the %R decreased as the Cr^{3+} ion concentration increased relative to the %IEC. However, the drop was not seen until after 50% saturation was achieved at the higher pHs, 2 and 3. This is again believed to be a result of the higher charge density of the Cr^{3+} cation.

The affinities of the hydrated and dry phases of all three materials for Cr^{3+} are shown in Tables 9 and 10. Like with La^{3+}, there seems to be a slightly higher affinity for Cr^{3+} when the exchangeable cation is larger, with the order of affinity following the general trend Cs-ZrP ≥ Rb-ZrP ≥ K-ZrP. This is the most pronounced in pH 2 at 50% IEC system, but can also be observed under several of the other conditions studied. This again, is most likely caused by a combination of the weaker ionic interaction of the more diffuse, larger monovalent cations, as well as the lower diffusion barrier caused by the larger d-spacing of the Zr layers. Likewise, the hydrated phase of a given ZrP material continues to have a slightly stronger affinity for Cr^{3+} over the dry phase, albeit subtly. The less pronounced preference of the hydrated phase with Cr^{3+} is believed to be a result of the small ionic radii of Cr^{3+}, so even with the smaller d-spacing of the dry phases, there is not a large diffusion barrier. The same muting between the pH 3 and pH 2 systems is believed to be due to the high charge density of the Cr^{3+}, where a higher H^+ concentration is needed to outcompete the Cr^{3+} at the PO^- active sites, as discussed earlier.

Leaching of the La^{3+} and Cr^{3+} loaded alkali metal substituted alpha-zirconium phosphate phases

One important aspect of developing a delivery mechanism for radionuclides is understanding how tightly the ions are bound. For this, the La^{3+} and Cr^{3+} loaded A-ZrP materials were contacted with various leaching solutions for 24 h. As shown in Table 11, the La^{3+} is bound quite strongly and retained in

(1.22 Å (ref. 28)), so the charge density is significantly higher for the Cr^{3+}, leading to it being more strongly bound to the PO^- active sites. Once the pH was reduced to pH 1, the sorp-

Table 9 Summary of the uptake of Cr^{3+} ions from solution present at 25%, 50%, 75%, and 100% of the IEC for the hydrated K-ZrP, Rb-ZrP, and Cs-ZrP phases

Sample	% IEC	pH 3 K_d (mL g^{-1})	pH 2 K_d (mL g^{-1})	pH 1 K_d (mL g^{-1})
K-ZrP	25%	3200 ± 800	1900 ± 200	280 ± 30
	50%	2200 ± 500	2000 ± 800	19 ± 3
	75%	34 ± 2	31 ± 2	17 ± 8
	100%	13 ± 4	13 ± 3	9 ± 3
Rb-ZrP	25%	4000 ± 3000	2800 ± 200	380 ± 20
	50%	3900 ± 600	2100 ± 200	38 ± 5
	75%	48 ± 4	33 ± 2	18 ± 5
	100%	17 ± 2	20 ± 10	14 ± 3
Cs-ZrP	25%	4800 ± 400	3000 ± 1000	30 ± 20
	50%	5000 ± 4000	2000 ± 1000	8 ± 8
	75%	39 ± 3	23 ± 1	5 ± 5
	100%	14 ± 1	13 ± 3	3 ± 2

Table 10 Summary of the uptake of Cr^{3+} ions from solution present at 25%, 50%, 75%, and 100% of the IEC for the dry K-ZrP, Rb-ZrP, and Cs-ZrP phases

Sample	% IEC	pH 3 K_d (mL g^{-1})	pH 2 K_d (mL g^{-1})	pH 1 K_d (mL g^{-1})
K-ZrP	25%	2600 ± 800	3400 ± 900	100 ± 20
	50%	2200 ± 600	1300 ± 100	16 ± 2
	75%	14 ± 2	13 ± 3	9 ± 1
	100%	9 ± 1	8 ± 1	7 ± 2
Rb-ZrP	25%	2700 ± 700	2100 ± 400	140 ± 30
	50%	2300 ± 300	2100 ± 200	44 ± 6
	75%	27 ± 4	27 ± 7	16 ± 1
	100%	10 ± 4	11 ± 3	9 ± 2
Cs-ZrP	25%	2800 ± 300	4000 ± 3000	20 ± 6
	50%	3000 ± 2000	3000 ± 1000	13 ± 4
	75%	22 ± 7	30 ± 20	8 ± 2
	100%	17 ± 6	13 ± 1	4 ± 2

the A-ZrP materials in the carbonate buffer, phosphate buffer, the HEPES buffer, and the 0.1 mM EDTA solution. Once the EDTA concentrations in increased to 1.0 M, La^{3+} begins to leach out of the Rb-ZrP and Cs-ZrP materials, 5–6% and 3–4%, respectively. While the K-ZrP materials do not show any sign of La^{3+} release. Upon further increasing the EDTA concentration to 10 mM, a significant portion of the La^{3+} is removed in all cases, 36–46%.

The binding of the Cr^{3+} was shown to be much stronger than that of La^{3+} (see Table 12), where no leaching was observed in any of the systems studied. This aligns with the Cr^{3+} having a much larger charge density, making the electrostatic interaction with the phosphate groups of the layers more stable.

Conclusion

The conversion of the pristine α-ZrP to the alkali metal phases K-, Rb-, and Cs-ZrP was successfully carried out *via* treatment with metal hydroxide/chloride solutions. Once converted, a portion of the materials were dried to generate a hydrated and dry phase for each counter cation. A full suite of characterization techniques, including XRPD, TGA, FTIR, SEM, TEM, and XPS, was utilized to confirm that the materials stayed intact, with only the expansion of the Zr layers. The effect on the ion exchange behavior of converting pristine α-ZrP to the alkali metal phases K-, Rb-, and Cs-ZrP, as well as hydrated *vs.* the dry phases, has been studied. In all cases, replacing the H^+ with K^+, Rb^+, or Cs^+ significantly improved the ion exchange behavior with both a trivalent f-block metal, La^{3+}, and a trivalent d-block metal, Cr^{3+}, with near quantitative removal of the M^{3+} cations from solution when the pH ≥2 and the trivalent

Table 11 Summary of leaching results with the La^{3+} loaded A-ZrP materials

Sample	Carbonate pH 7.4	Phosphate pH 7.2	HEPES pH 7.4	0.1 mM EDTA pH 7.2	1.0 mM EDTA pH 7.3	10 mM EDTA pH 7.2
K-ZrP hydrated	≤0.5%	≤0.5%	≤0.5%	≤0.5%	≤0.5%	40 ± 1%
K-ZrP dry	≤0.5%	≤0.5%	≤0.5%	≤0.5%	≤0.5%	39 ± 1%
Rb-ZrP hydrated	≤0.5%	≤0.5%	≤0.5%	≤0.5%	5.9 ± 0.2%	46 ± 1%
Rb-ZrP dry	≤0.5%	≤0.5%	≤0.5%	≤0.5%	5.3 ± 0.3%	46 ± 1%
Cs-ZrP hydrated	≤0.5%	≤0.5%	≤0.5%	≤0.5%	3.5 ± 0.2%	36 ± 1%
Cs-ZrP dry	≤0.5%	≤0.5%	≤0.5%	≤0.5%	3.2 ± 0.1%	37 ± 1%

Table 12 Summary of leaching results with the Cr^{3+} loaded A-ZrP materials

Sample	Carbonate pH 7.4	Phosphate pH 7.2	HEPES pH 7.4	0.1 mM EDTA pH 7.2	1.0 mM EDTA pH 7.3	10 mM EDTA pH 7.2
K-ZrP hydrated	≤0.5%	≤0.5%	≤0.5%	≤0.5%	≤0.5%	≤0.5%
K-ZrP dry	≤0.5%	≤0.5%	≤0.5%	≤0.5%	≤0.5%	≤0.5%
Rb-ZrP hydrated	≤0.5%	≤0.5%	≤0.5%	≤0.5%	≤0.5%	≤0.5%
Rb-ZrP dry	≤0.5%	≤0.5%	≤0.5%	≤0.5%	≤0.5%	≤0.5%
Cs-ZrP hydrated	≤0.5%	≤0.5%	≤0.5%	≤0.5%	≤0.5%	≤0.5%
Cs-ZrP dry	≤0.5%	≤0.5%	≤0.5%	≤0.5%	≤0.5%	≤0.5%

metal ion content was ≤50% of the material IEC. At lower pH values, the excess H^+ in solution outcompetes the La^{3+} cations and, to a lesser extent, the Cr^{3+} cations. When the metal content is >50% of the material IEC, the efficiency of the materials is due to the majority of the active sites being occupied and materials nearing saturation. Once intercalated in the ZrP materials, the ions are bound strongly and do not show any leaching in either a carbonate, phosphate, or HEPES buffer. There was also no observable leaching in the challenge with EDTA up to a concentration of 0.1 mM for La^{3+} and 10 mM for Cr^{3+}. Again, this is advantageous when considering the ZrP materials as a potential radionuclide delivery mechanism, retaining the ions under physiological conditions.

Taking these results in the context of a radionuclide delivery vehicle, where the radionuclide is available in trace amounts (nM range and below) and the labeling conditions are expected to be mild, the A-ZrP materials have considerable potential. In this way, small amounts of the ZrP materials (10s of μg quantities) could be used to deliver nmol quantities of the radionuclide.

Conflicts of interest

The authors declare no financial interests.

Data availability

The datasets generated during and/or analyzed during the current study are available from the corresponding author on reasonable request.

Acknowledgements

This report was prepared as an account of work sponsored by an agency of the United States Government. Neither the United States Government nor any agency thereof, nor any of their employees, makes any warranty, express or implied, or assumes any legal liability or responsibility for the accuracy, completeness, or usefulness of any information, apparatus, product, or process disclosed, or represents that its use would not infringe privately owned rights. Reference herein to any specific commercial product, process, or service by trade name, trademark, manufacturer, or otherwise does not necessarily constitute or imply its endorsement, recommendation, or favoring by the United States Government or any agency thereof. The views and opinions of authors expressed herein do not necessarily state or reflect those of the United States Government or any agency thereof.

References

1 T. G. Chan, E. O'Neill, C. Habjan and B. Cornelissen, *J. Nucl. Med.*, 2020, **61**, 1544–1552.

2 B. J. Burkett, D. J. Bartlett, P. W. McGarrah, A. R. Lewis, D. R. Johnson, K. Berberoglu, M. K. Pandey, A. T. Packard, T. R. Halfdanarson, C. B. Hruska, G. B. Johnson and A. T. Kendi, *Radiol.: Imaging Cancer*, 2023, **5**, e220157.

3 N. Sun, T. Wang and S. Zhang, *J. Nanobiotechnol.*, 2024, **22**, 728.

4 M. L. Matson, C. H. Villa, J. S. Ananta, J. J. Law, D. A. Scheinberg and L. J. Wilson, *J. Nucl. Med.*, 2015, **56**, 897–900.

5 J. V. Rojas, J. D. Woodward, N. Chen, A. J. Rondinone, C. H. Castano and S. Mirzadeh, *Nucl. Med. Biol.*, 2015, **42**, 614–620.

6 M. Toro-González, A. N. Dame, C. M. Foster, L. J. Millet, J. D. Woodward, J. V. Rojas, S. Mirzadeh and S. M. Davern, *Nanoscale*, 2020, **12**, 9744–9755.

7 M. Toro-González, A. Peacock, A. Miskowiec, D. A. Cullen, R. Copping, S. Mirzadeh and S. M. Davern, *J. Nanotheranostics*, 2021, **2**, 33–50.

8 M. W. Ambrogio, M. Toro-González, T. J. Keever, T. E. McKnight and S. M. Davern, *ACS Appl. Nano Mater.*, 2020, **3**, 10565–10570.

9 J. D. Einkauf, L. H. Ortega, S. M. McDeavitt and J. D. Burns, *Solvent Extr. Ion Exch.*, 2020, **38**, 612–628.

10 L. Ondrak, K. O. Fialova, M. Vlk, K. Stamberg, F. Bruchertseifer, A. Morgenstern and J. Kozempel, *Materials*, 2023, **16**, 5732.

11 A. Clearfield and J. A. Stynes, *J. Inorg. Nucl. Chem.*, 1964, **26**, 117–129.

12 A. Díaz, V. Saxena, J. González, A. David, B. Casañas, C. Carpenter, J. D. Batteas, J. L. Colón, A. Clearfield and M. D. Hussain, *Chem. Commun.*, 2012, **48**, 1754–1756.

13 J. M. Troup and A. Clearfield, *Inorg. Chem.*, 1977, **16**, 3311–3314.

14 A. Clearfield and G. D. Smith, *Inorg. Chem.*, 1969, **8**, 431–436.

15 V. Saxena, A. Diaz, A. Clearfield, J. D. Batteas and M. D. Hussain, *Nanoscale*, 2013, **5**, 2328–2336.

16 A. Díaz, B. M. Mosby, V. I. Bakhmutov, A. A. Martí, J. D. Batteas and A. Clearfield, *Chem. Mater.*, 2013, **25**, 723–728.

17 B. M. Mosby, A. Díaz, V. Bakhmutov and A. Clearfield, *ACS Appl. Mater. Interfaces*, 2014, **6**, 585–592.

18 A. F. Mejia, A. Diaz, S. Pullela, Y. W. Chang, M. Simonetty, C. Carpenter, J. D. Batteas, M. S. Mannan, A. Clearfield and Z. D. Cheng, *Soft Matter*, 2012, **8**, 10245–10253.

19 V. I. Bakhmutov and A. Clearfield, *J. Phys. Chem. C*, 2016, **120**, 19225–19233.

20 M. Pica, S. Lixi, A. Donnadio, M. Casciola and M. Nocchetti, *ChemNanoMat*, 2023, **9**, e202300276.

21 M. Casciola, D. Capitani, A. Donnadio, G. Munari and M. Pica, *Inorg. Chem.*, 2010, **49**, 3329–3336.

22 A. Díaz, A. David, R. Pérez, M. L. González, A. Báez, S. E. Wark, P. Zhang, A. Clearfield and J. L. Colón, *Biomacromolecules*, 2010, **11**, 2465–2470.

23 S. Ghosh, A. Sharma and G. Talukder, *Biol. Trace Elem. Res.*, 1992, **35**, 247–271.

24 M. Pica, A. Donnadio and M. Casciola, *Coord. Chem. Rev.*, 2018, **374**, 218–235.

25 A. Díaz, M. L. González, R. J. Pérez, A. David, A. Mukherjee, A. Báez, A. Clearfield and J. L. Colón, *Nanoscale*, 2013, **5**, 11456–11456.

26 L. Kullberg and A. Clearfield, *J. Phys. Chem.*, 1981, **85**, 1585–1589.

27 G. Alberti, *Acc. Chem. Res.*, 1978, **11**, 163–170.

28 E. Mauerhofer, K. P. Zhernosekov and F. Rösch, *Radiochim. Acta*, 2003, **91**, 473–477.